

MODELLING THE DUST-LADEN MARTIAN BOUNDARY LAYER

Richard Davy, Peter A. Taylor, Wensong Weng and P-Y Li

Centre for Research in Earth and Space Science, York University, 4700 Keele St, Toronto, Ontario, M3J 1P3, Canada

1. Abstract

The NASA/University of Arizona Phoenix mission is scheduled to land at 70 degrees North on Mars in late May. The MET package provided primarily by the Canadian Space Agency will include a vertically pointing dual wavelength lidar to study distributions of dust and cloud. In particular we plan to use the lidar returns to determine the depth of the afternoon boundary layer, on the assumption that there will be a significant drop in the dust concentration at that level.

The recent paper by Taylor et al (Boundary-Layer Meteorology, 125, 305-328) describes one approach to predicting boundary-layer depth based on separate models of diurnal cycles of the Martian boundary layer and of the transport, settling and diffusion of size distributed dust. The conclusion of that modelling study was that it would be possible to determine the boundary-layer depth both when dust was being advected into the region from dust storms initiated elsewhere or in strong wind situations, from dust raised locally. We also noted that "Further work is needed to couple the boundary-layer and dust models and to make quantitative comparisons with data to be collected during the Phoenix mission."

In the present paper we have refined the dust optical properties and coupled the two models. While results are generally similar to those obtained with the uncoupled model we do see an increase in the maximum boundary-layer height from ~2.4km (uncoupled) to ~3km (coupled) in our reference case. While we are unlikely to have extensive data from the Phoenix lander in time for the June symposium we will present model calculations for a range of anticipated scenarios.

2. Introduction

Phoenix, the first NASA scout mission, launched in August 2007 and should land on the northern polar region of Mars, at approximately 70 degrees North, in May 2008. The Canadian Space Agency provided the meteorological instrument package (MET) for the Phoenix lander which includes a dual wavelength (532, 1064 nm) vertically pointing lidar. One of the lines of investigation for the Phoenix mission is whether the lidar will be

able to detect the afternoon convective boundary-layer height. This will depend upon the sharpness of the gradient in particle concentration at the top of the boundary layer.

Atmospheric dust has a large impact on the radiative heating, and therefore the dynamical structure, of the Martian atmosphere (e.g. Tomasko et al., 1999; Pollack et al., 1995). To determine the radiative effects we need to know the optical properties and size distribution of the suspended dust. Model runs were completed for two scenarios: the decay of a dust storm with the dust assumed to have been advected from a remote source (Scenario A) and the local generation of dust lifted from the surface (Scenario B). Model runs were completed for geostrophic wind speeds of 10, 20 (A) and 35 ms⁻¹ (B).

3. The model

The PBL model is an adaption of the 1-D model of Savijarvi et al. (2004) with E-I turbulence closure. This is a 1.5 order turbulence closure with a prognostic equation for turbulent kinetic energy and a diagnostic equation for turbulence length scale. All scenarios used a surface pressure of 6.75 hPa; albedo of 0.21 and a surface emissivity of 0.96 as in Weng et al. (2006). In order to match the conditions at the Phoenix lander site we used latitude 70° N and an initial solar longitude of 90°. The model is run over 30 Martian days (sols) with a time step of 5 sec. For the vertical domain the same log-linear coordinate transform of Weng et al. (2006) was used but the number of vertical grid points was increased to 241 over a 30km domain. The model is moist and has the potential to form water-ice clouds. These, as well as some surface ice, were seen in most model scenarios. Ice is assumed to form when the relative humidity with respect to ice exceeds 100%. The soil is modelled through a 5 level thermal diffusion scheme with an assumed thermal conductivity of 0.12 Wm⁻¹K⁻¹ and volumetric heat capacity of 0.8 MJ m⁻³ K⁻¹ (Savijarvi 1999). The soil wetness is held constant at 0.003%.

Initial conditions in terms of wind, temperature and TKE profiles were obtained from an uncoupled model. Runs were completed where the PBL model used a fixed optical depth profile and constant solar longitude. The model is run for 10 sols at which time a closed diurnal cycle of wind, temperature and TKE is obtained. The profiles of wind speed, temperature and TKE parameters at 00h on the final sol are then used as the initial conditions for the coupled model.

Corresponding author address: Richard Davy, York University, Dept. of Earth and Space Science, Toronto, ON; e-mail: rajd84@yorku.ca

The surface temperature is taken from the diurnally averaged Pathfinder results (Savijarvi 1999). Note that the Dry Adiabatic Lapse Rate (Γ) on Mars is about 4.5 K km^{-1} .

The numerical discretisation of the equations follows the method described by Taylor et al. (2007), hereafter referred to as T07, but with 241 grid points spread over a vertical domain from 1m to 30km. To model the dust distribution 121 particle size bins were created spread evenly over a logarithmic scale from radius of 0.1 to $10 \mu\text{m}$. Note, hereafter particle size refers to radius e.g. “ $1 \mu\text{m}$ particles” refers to particles with a radius of $1 \mu\text{m}$. For a given particle size, r , the flux of particles, F , (positive upwards) at some height, z , is given by:

$$F(r,z) = -w_p(r,z) N(r,z) - K_s(z) \frac{\partial N(r,z)}{\partial z} \quad (1)$$

where N is the particle number density; K_s is the eddy diffusivity and w_p is the settling velocity of the given particle size. At the upper boundary we specify $N(r, z_{\text{top}}) = 0$.

At each time step the PBL model is used to calculate the wind, temperature and eddy diffusivity profiles. These are then used by the dust component of the model to determine the new particle distribution. The particle size distribution is then used to calculate the dust optical depth profile which is then used at the next time step by the PBL model to determine the radiative heating or cooling associated with the dust.

The initial dust size distribution profile is described by a gamma distribution where

$$\frac{N(r,z)}{C} = \left(\frac{r}{a}\right)^{\frac{1-3b}{b}} \exp(-r/ab) \exp(-z/H) \quad (2)$$

Here the effective radius, a , is taken to be $1.6 \mu\text{m}$ and the effective variance, b , is 0.2 (Tomasko et al, 1999). The constant C is a scaling factor which fixes the number density to a specific optical depth. The top boundary condition is $N(r, z_{\text{top}}) = 0$. Here we take the initial dust profile to have a visible optical depth of 0.5 with a corresponding value for C of $1.74 \times 10^{14} \text{ m}^{-4}$. The dust is vertically distributed with a scale height, H , of 11.3 km, equal to the gas scale height at initial conditions: a constant mixing ratio. This is consistent with the results from the Phobos mission (Moroz et al. 1993).

3.2 Surface lifting

Since dust lifting by dust devils cannot readily be integrated into a 1D model, surface lifting of dust is restricted to surface wind stress. Analysis

indicated that the minimum threshold for surface friction velocity (u_{t_min}) of 1.3 ms^{-1} (T07) is exceeded at geostrophic wind speeds greater than 30 ms^{-1} . Thus, as in T07, the surface boundary condition takes the form:

$$F_0 = -w_d N \quad \text{for } u_{s0} \leq u_{st} \\ = -w_d N + \alpha_g (u_{s0}/u_{st})^3 (u_{s0}/u_{st} - 1) \quad \text{for } u_{s0} > u_{st} \quad (3)$$

for particle number density, $N(r,z)$; deposition velocity, $w_d(r)$ and surface friction velocity, u_{s0} . Here $\alpha_g(r)$ describes the dust source function such that:

$$\alpha_g(r) = u_{*t}(r) C (r/a)^{(1-3b)/b} \exp(-r/ab) \quad (4)$$

with a , b and C taking the same values as used in Equation 2. The threshold friction velocity for particles of radius r , $u_{*t}(r)$ is determined from the iterative method described by Equation 15 of T07 with the aforementioned minimum, u_{*t_min} .

3.3 Optical properties of the dust

In the previous work (Taylor et al. 2007) the extinction efficiency Q_{ext} was taken from Ockert-Bell et al. (1997) which provides values of Q_{ext} for a variety of wavelengths based on the size distribution presented by Pollack et al. (1995) where $a=1.85 \mu\text{m}$ and $b=0.51$. While this is different from the values taken here ($a=1.6 \mu\text{m}$, $b=0.2$) a comparison of Q_{ext} for different particle size distributions by Pollack et al. (1995) indicates that Q_{ext} has a much stronger variation with wavelength than with size distribution. For our purposes Q_{ext} will be treated as constant with respect to particle size distribution with the appropriate values being taken from Ockert-Bell (1997). While the particle size distribution will alter over the course of a model run, owing to the varied settling rates of different particle sizes, this variation is not strong enough to warrant a time variation of Q_{ext} . A model run was completed using the Bohren-Huffman Mie scattering theory where values of Q_{ext} could be determined for each particle size. These values of Q_{ext} were determined based on the assumption the particles are spherical. While the size distribution altered over the course of a 30 sol model run this did not significantly alter the particle size weighted value of Q_{ext} .

The asymmetry parameter, g , and the single scattering albedo, ω , are taken to be 0.7 and 0.9 respectively (Savijarvi et al. 2004). These values are weighted to the solar spectrum and a dust distribution with $a=1.6 \mu\text{m}$, $b=0.5$ (Tomasko et al. 1999). These parameters are used to determine the shortwave flux from dust by the two-stream method.

3. Lidar

To illustrate how we might determine the lidar backscatter in a sample case we follow the method of Murphy and Hawley (1993) where the backscatter coefficient, β_π , for a range of particle sizes can be determined by:

$$\beta_\pi(\lambda, z) = \frac{1}{k^2} \int S_{11}(\lambda, \pi, r) N(r, z) dr \quad (5)$$

S_{11} is the Mie coefficient for scattering by a particle of radius r , at wavelength λ to angle π (180°); $N(r, z)$ is the number density of particles of radius r at height z and k is the wavenumber, $2\pi/\lambda$. The Bohren-Huffman Mie scattering theory was used to obtain the relevant values of S_{11} for each particle size. Note that here we assume the particles are spherical and homogenous. Values for the refractive index (n_r) and complex index of refraction (n_i) were interpolated to the Phoenix lidar wavelengths from the data of Ockert-Bell et al. (1997). At 532nm we have $n_r=1.518$ and $n_i=0.0068$ and at 1064nm we have $n_r=1.501$ and $n_i=0.0032$. Thus integrating over our chosen size range gives us a vertical profile of the backscatter coefficient. Note that the backscatter coefficient will be constant within an ideal well-mixed boundary layer. In practice it is unlikely that the larger particles, with their large settling velocities, will be well-mixed within the boundary layer so we should expect some decay in the backscatter coefficient within this region.

4. Results / Discussion

4.1 A) Decay of a dust storm

The coupled model runs were started at 00h with the dust profile of Equation 2. Our standard scenario has an initial surface optical depth, τ_{s0} , of 0.5; a roughness length, z_0 , of 0.01m; a geostrophic wind, U_g , of 10 ms^{-1} , a dust scale height, H , of 11.3km and an initial environmental lapse rate, γ , of 0 K km^{-1} . Table 1 indicates the variation in the above properties that was explored, discussed below. Our standard scenario, A1, was run over 90 sols; all other scenarios were run over 30 sols.

Figure D shows the temperature and potential temperature profiles at various times on the 1st and 30th sols of run A1. The temperature and diurnal cycle of the temperature in the atmosphere above the PBL are seen to decrease. That is to be expected as the reduced dust concentration in this part of the atmosphere will reduce the local heating. This can be seen in the temperature profile of Figure D where the diurnal cycle in temperature at 6 km drops from $\sim 6 \text{ K}$ (1st sol) to $\sim 4 \text{ K}$ (30th sol) and the diurnal mean at this height drops from $\sim 224.5 \text{ K}$ (1st sol) to $\sim 213.3 \text{ K}$ (30th sol).

As dust settles out over the course of a model run, in a similar fashion to that discussed in T07, Figure 6, we see the surface optical depth decrease and the optical depth profile change shape, see Fig A. Note, a linear decay of optical depth with height is indicative of a well-mixed layer. Here we also see how the contribution to the surface optical depth from each particle size bin varies over time. As expected with the larger particles settling out faster the smaller particles become of increasing importance to the total optical depth. After 30 sols the surface optical depth has reduced to 0.24 and there is a non-negligible optical depth to a height of 15 km. To explore the conditions with dust entirely within the boundary layer the standard model was run for 90 sols. After 90 sols the surface optical depth has decreased to 0.056 and all but the smallest particles have settled into the boundary layer which is seen in the near-zero optical depth above the boundary layer (Figure A). The diurnal variation of the optical depth profile is small and, since in these cases the lower boundary can only be a sink for particles, the surface optical depth can only decrease. As the radiatively active dust settles out, the proportion of solar energy reaching the surface increases. Note that between the 30th and 60th sols the increase of surface solar radiation from dust settling is balanced by the decrease due to solar longitude. After the 60th sol the effect of solar longitude dominates over any further settling of dust so the surface solar radiation decreases.

This increase in surface heating increases convection and vertical heat transport which gives us an increase in the maximum afternoon boundary-layer height (Figure B). Figure C illustrates the correlation between afternoon boundary-layer height and surface optical depth for scenarios with a geostrophic wind of 10 ms^{-1} and initial surface optical depth of 0.5, 1 and 5. This correlation is in contrast to the T07 results where this feed back is not accounted for.

Over the course of a model run the atmospheric dust loading decreases and the surface temperature increases, as expected from the increased solar radiation reaching the surface.

There is not a significant diurnal cycle in the concentration of particles less than $1 \mu\text{m}$; they remain well-mixed below the maximum boundary layer height. This can be attributed to their small settling velocities ($10\text{-}100 \text{ m sol}^{-1}$): the particles do not have sufficient time to settle significantly between convective mixings. The larger particles ($5\text{-}10 \mu\text{m}$) do settle significantly outside of convective mixing ($\sim 2.5 \text{ km sol}^{-1}$) and as such they act as a better tracer of boundary layer growth, although they will not settle sufficiently quickly to follow the boundary layer height in the early evening. However, after 30 sols the concentrations of these particles are many orders of magnitude smaller than the initial conditions

and thus will not contribute greatly to the lidar backscatter profile.

Figure E illustrates the backscatter coefficient profile, at a wavelength of 532nm, at 1200 and 1700 on the 30th and 90th sols. On the 30th sol there is a sharp, approximately 20%, drop in the backscatter at the top of the dust-laden air and the dust-layer top, corresponding to the maximum boundary-layer height reached in the afternoon (at 1700). There is some diurnal variation in the top of this high backscatter layer which traces the boundary layer growth, as illustrated in Figure E, but the intensity variation is small and the height fluctuation may not be detectable with the limited number of lidar soundings anticipated on a typical sol during the Phoenix mission. However, provided our assumptions about the mixing processes are correct, these results do indicate that the lidar should be fully capable of determining the afternoon boundary-layer depth in the 30 sol scenario even though there is still a significant dust loading above the boundary layer.

4.25 Uncoupled model comparison

This model was applied to observations of the 1977B dust storm encountered by Viking Lander 1. Murphy et al. (1990) used a 1-D model to simulate the decay of the 1977A and 1977B dust storms. This model used height-independent eddy diffusivity with an isothermal and static atmosphere. We set the initial conditions at surface pressure of 8.3 mbar; surface temperature of 220 K; latitude of 22.3°N; optical depth of 6 and solar longitude of 273°, as in Murphy et al. (1990). The initial lapse rate was determined, from an uncoupled run, to be -0.5 K km⁻¹. Following the analysis of Pollack et al. (1995) we took the effective radius of the dust distribution as 1.52 μm ; the effective variance as 0.5 and the asymmetry parameter as 0.6. These values come from an earlier high optical depth (=1.93) period at solar longitude 208.1. All other constants remained the same. The model is run for 200 sols from sol 320 to 520 of the Viking Lander 1 mission. Figure F illustrates the decay of optical depth over this period for constant geostrophic wind speed of 10 ms⁻¹. There is a good fit to the data for most of the decay period although the model produces lower than observed values for the last 30 sols of the run. Murphy et al. (1990) used a constant eddy diffusivity with runs completed for $K_m = 0$ and 10³ m²s⁻¹ for spherical particles. The results presented here are an improved fit to the data compared to these two cases.

4.3 B) Surface as a source of dust

With a geostrophic wind speed of 35 ms⁻¹ the surface acts as a source for dust, as described by equations 3 and 4, when the surface friction velocity exceeds the threshold for lifting by wind shear. This typically occurs in the morning between 0900 and 1200. During the remainder of the sol the surface is only a sink for particles. The values for z_0 , H and γ are the same as scenario

A1. Two model runs were completed for initial optical depths (τ_0) of 0 and 0.5 (model run B1 and B2 respectively) using a dust profile described by Equation 2 and source function of Equation 3 and 4. Note that, while we assume an unlimited dust source, the mean surface depth required to supply the determined dust profile is less than 1 μm . Strong entrainment, ratio of entrainment to surface heat flux of -0.2, is seen during the growth of the convective boundary layer (CBL) in all model runs. This was not seen in scenario A, where there was negligible entrainment on the 30th sol. The strong entrainment is a consequence of the large gradient in dust concentration at the CBL interface due to dust lifting. In run B1 there is dust present above the boundary layer on the 30th sol, seen in the backscatter of figure G (a). This is a consequence of the initial conditions: without atmospheric dust present on the first sol the boundary layer reaches 6.5km. Small dust particles are lifted to this height and, because of their small settling velocities, they remain there. On subsequent sols the boundary-layer height is reduced due to the presence of dust in the atmosphere, thus on the 30th sol we see dust above the boundary layer.

The surface optical depth on the 30th sol of run B2 was greater than B1 with mean values of 0.43 and 0.33 respectively. This is due to the low settling velocity of the large concentration of small particles above the boundary layer in B2. The duration of dust lifting in a given sol is similar for runs B1 and B2, occurring between 0900 and 1230. In both model runs the column-integrated number density of the larger particles settles to a near-closed diurnal cycle within 10 sols with similar values for both runs e.g. mean values of 4.4 and 3.6 cm⁻² on the 30th sol for B1 and B2 respectively. Figure G illustrates the profile of the backscatter coefficient at various times on the 30th sol for each model run. We see a decrease in backscatter at the maximum CBL height at 1600 similar to that seen in scenario A. In both model runs the afternoon growth of the CBL is reasonably defined by the backscatter. The backscatter coefficient is not as constant within the CBL as in scenario A. This is due to the heavy dust loading near the surface preventing the CBL from being well-mixed.

5. Conclusions

We have presented results from a coupled model combining a 1D eddy diffusion dust model with a 1D E-I closure PBL model. Absorption of solar radiation by the dust plays an important role and represents an improvement over earlier PBL calculations with a prescribed dust distribution. Results pertinent to the Phoenix lander are presented. From the predicted dust distributions and lidar backscatter we can anticipate that the onboard Phoenix lidar should be able to detect the afternoon maximum boundary layer height but is unlikely to be able to accurately determine boundary-layer growth and collapse over the diurnal cycle.

For more details see:

<http://www.yorku.ca/pat/research/Phoenix.html>

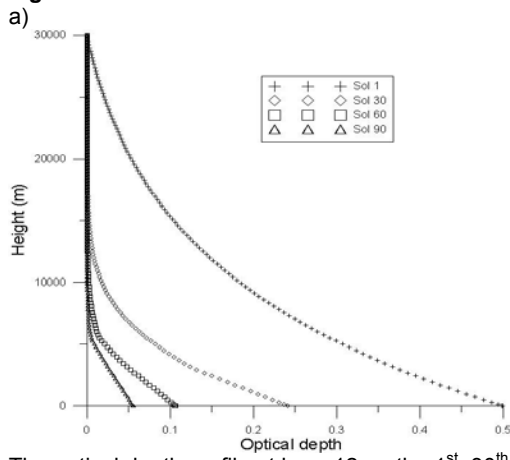
6. Acknowledgements

Financial support for this study has been provided through a Canadian Space Agency, Space Science Enhancement Program grant.

References

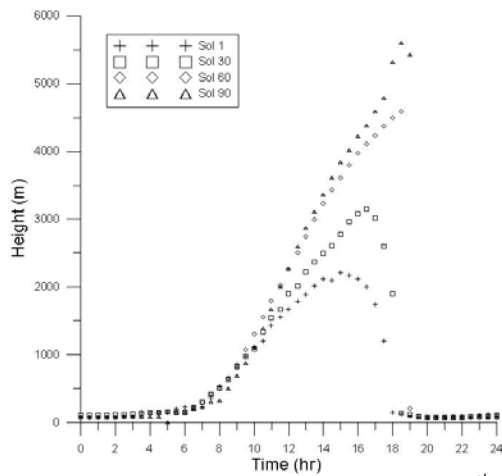
- Colburn, D.S., Pollack, J.B. and Haberle, R. M., 1989, Diurnal Variations in Optical Depth at Mars, *Icarus*, **79**, 159-189
- Michelangeli, D.V., Toon, O.B., Haberle, R.M. and Pollack, J.B., 1993, Numerical simulations of the formation and evolution of water ice clouds in the Martian atmosphere, *Icarus*, **102**, 261-285
- Moroz, V.I., Gektin, Y.M., Naraeva, M.K., Selivanov, A.S. and Titov, D.V., Aerosol vertical profile on Mars from the measurements of thermal radiation on the limb, *P&SS*, **42**, 10, 831-845
- Murphy, D.L. and Hawley, J.E., Lidar detection of levitated lunar dust, 1993, *Proc. SPIE*, **1936**, 182-190
- Murphy, J.R., Toon, O.B., Haberle, R.M. and Pollack, J.B., 1990, Numerical simulations of the decay of Martian dust storms, *J. Geophys. Res.*, **95**, 14629-14648.
- Ockert-Bell, M.E., Bell, J.F. III, Pollack, J.B., McKay, C.P. and Forget, F., 1997, Absorption and scattering properties of the Martian dust in the solar wavelengths, *J. Geophys. Res.*, **102**, 9039-9050
- Pollack, J.B., Ockert-Bell, M.E. and Shepard, M.K., 1995, Viking Lander image analysis of Martian atmospheric dust, *J. Geophys. Res.*, **100**, 5235-5250
- Savijarvi, H., A model study of the atmospheric boundary layer in the Mars Pathfinder lander conditions, 1999, *Q. J. R. Meteorol. Soc.*, **125**, 483-493
- Savijarvi, H., Maattanen, A., KauHannen, J. and Harri, A-M., 2004, Mars Pathfinder: New data and new model simulations, *Q. J. R. Meteorol. Soc.*, **130**, 669-683
- Smith, P.H. et al., 1997, Results from the Mars Pathfinder Camera, *Science*, **278**, 1758
- Taylor, P.A., Li, P-Y., Michelangeli, D.V., Pathak, J. and Weng, W., 2007, Modelling dust distributions in the atmospheric boundary layer on Mars, *Boundary-Layer Meteorol.*, **125**, 305-328
- Tomasko, M.G., Doose, L.R., Lemmon, M., Smith, P.H. and Wegryn, E., 1999, Properties of dust in the Martian atmosphere from the Imager on Mars Pathfinder, *J. Geophys. Res.*, **104**, 8987-9007
- Weng, W. and Taylor, P., 2006, Modelling the one-dimensional stable boundary layer with an E-I turbulence closure scheme, *Boundary Layer Meteorol.*, **118**, 305-323

Figure A:



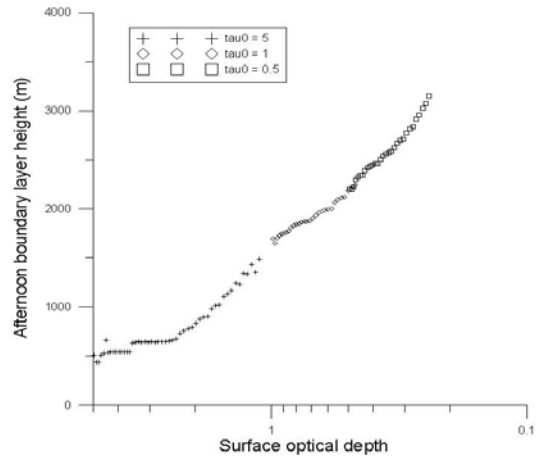
The optical depth profile at hour 12 on the 1st, 30th, 60th and 90th sols of run A1.

Figure B.



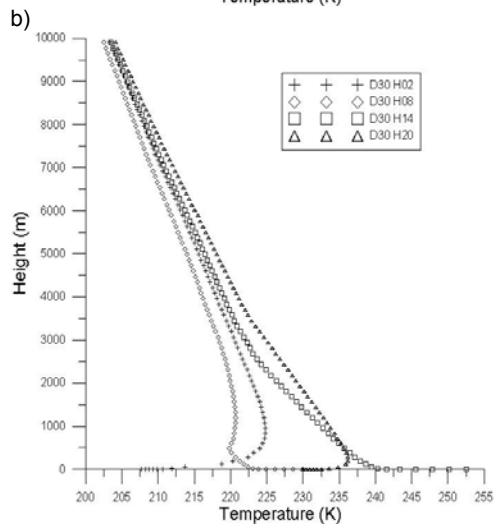
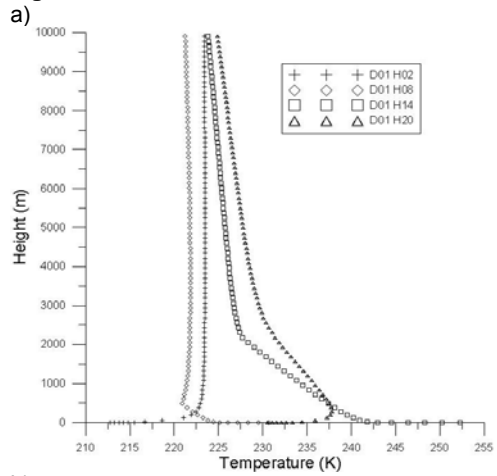
Diurnal cycle of boundary-layer height on the 1st, 30th, 60th and 90th sols of run A1.

Figure C.



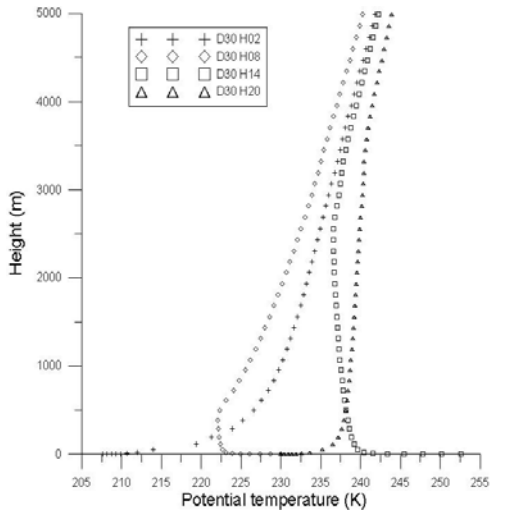
Afternoon boundary-layer height vs. surface optical depth.

Figure D:



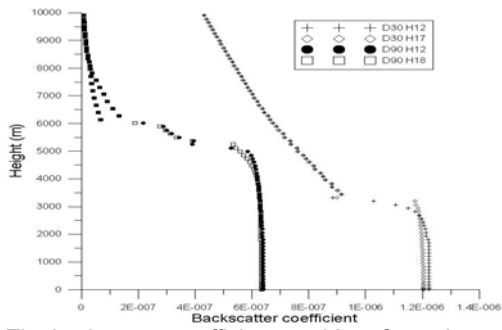
Temperature profiles at hours 02, 08, 14 and 20h on the a) 1st and b) 30th sols for run A1.

c)



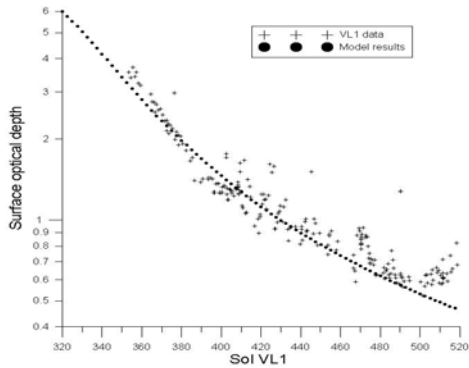
Potential temperature at 02, 08, 14 and 20h on the 30th sol

Figure E.



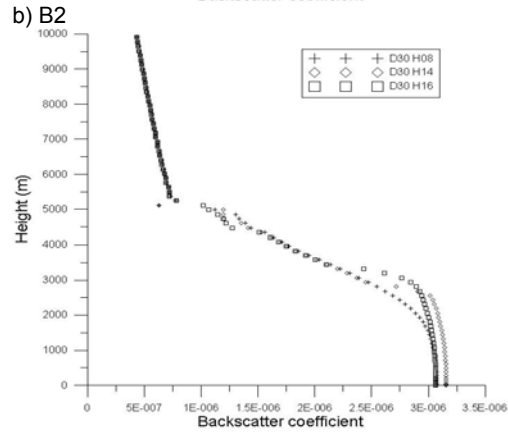
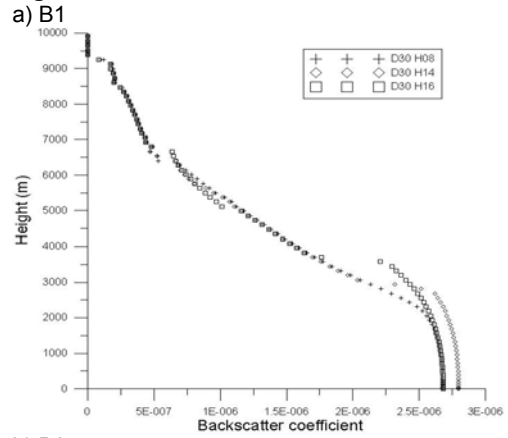
The backscatter coefficient at 532nm for various times on the 30th and 90th sols for run A1.

Figure F.



The surface optical depth for sols 320-520 of the Viking Lander 1 mission and the model results over this period for $U_g = 10\text{ms}^{-1}$

Figure G.



The backscatter coefficient at various times on the 30th sol for runs a)B1 and b)B2